Multistate Chipless RFID Tags for Robust Vibration Sensing

Ashkan Azarfar, Nicolas Barbot, Etienne Perret

Multi-state Chipless RFID Tags for Robust Vibration Sensing

Ashkan Azarfar, Nicolas Barbot, and Etienne Perret

***Abstract*—This paper introduces multi-state chipless RFID tags which can be utilized to enhance the vibration sensing range and reading robustness in real environments. The proposed multi-state chipless tag consists of a resonant scatterer trapped between two different dielectric layers, which causes the near-field boundary of the scatterer to be modulated during vibration and results in the appearance of multiple modulation states. The motion-induced near-field modulation provided by the multi-state chipless tag is much more effective than the natural Doppler modulation caused by vibration, which significantly increases the modulated portion of the backscattered power, and consequently, enlarges the sensing range. The backscattering from the vibrating multi-state chipless tag is studied using presented mechanical and electromagnetic models which are verified by simulations. The designed multi-state chipless tag is implemented and the concept is experimentally proven. The differential RCS of the vibrating multi-state chipless tag is 45 times greater than that of a vibrating classical chipless tag, which translates into an increase of factor 2.5 in the read range. The multi-state chipless RFID tag is utilized to successfully detect a sub-millimeter vibration through a wall in an indoor environment at low microwave frequencies, while the vibrating tag is located at 2.5 m distance.**

***Index Terms*—Backscatter modulation, Chipless Radio Frequency IDentification (RFID), differential Radar Cross Section (RCS), resonant scatterer, vibration sensing**

I. Introduction

NON-CONTACT vibration sensing based on coherent interferometry has been firstly established using optical approaches [1], [2]. Essentially in vibrometry based on Doppler coherent interferometry, the ratio of the vibration amplitude and the operating wavelength which defines the modulation index, is the most important parameter in defining the sensitivity (or the resolution) of the vibrometry. The optical vibrometry techniques provide a very high resolution due to their nanometer wavelength, while their performance is significantly affected by the environment where a line of sight (LOS) to the target is always needed. Microwave and millimeter-wave vibrometry [3] has been developed based on the same principle as optical methods (coherent interferometry) while the microwave signals can pass through different materials (except metals) which alleviates the LOS concern, although the resolution of the vibrometry is obviously lower in microwave compared to the optical approaches.

The microwave vibrometry has been employed in different applications such as fault detection in mechanical and civil structures [4]–[7], vital signs (respiration and heart beat rate) detection for health care monitoring [8]–[14], vocal vibration sensing for speech retrievement [15]–[18], and human gesture recognition [19]. Basically, all the microwave vibration sensors can be considered as a coherent Doppler radar which is realized either in Continuous Wave (CW) mode [4], [6], [7], [9]–[15] or Frequency Modulated Continuous Wave (FMCW) mode [5], [16], where the operating carrier frequency, the radar architecture, and the applied post-processing methods have important roles in the resolution, read range, and the accuracy of the vibration sensing. Generally, to achieve better sensitivity in most of the applications, high carrier frequencies (24 - 160 GHz) are preferred to design the sensing radar [5], [7], [9], [11], [16], [18], however, the implementation complexity and cost are also increased. Note that, although the vibration-induced phase modulation is greater at mm-waves (higher modulation indexes), the large free-space path loss at these high frequencies degrades significantly the sensing performance in term of read range (for a definite emitted power level) which cause that in most of the presented works [5], [7], [9], [11], [16], [18] the maximum sensing distance cannot be practically upper than 2.5 m. On the other hand, specific radar architectures [10], [11], [16] and post-processing techniques [5], [12]–[14], [17] have been also introduced to improve the vibration sensing performance in the mentioned applications at low carrier frequencies as 2.4 and 5.8 GHz [12]–[14], while the maximum read range in these cases is also limited by 0.5 m. Indeed, although the path loss is lowered as the carrier frequency decreased, the phase modulation index is also reduced significantly which degrades the sensitivity and the sensing range.

The key point worth to mention is that, in all these works [4]–[19], the only considered modulation source is the natural vibrational motion of the target object which induces a phase (Doppler) modulation on the backscattered wave. In fact, for a specific coherent Doppler radar system working at a defined carrier frequency and emitted power level, to detect an object (with defined RCS) vibrating with a fixed amplitude, the maximum reachable sensing range of the system is directly proportional to the modulated part of the backscattered power, which is fixed for the specific vibrating object and cannot be modified unless another non-linear or time-variant effect (in addition to the Doppler modulation caused by vibration) is added somehow into the target object.

Radio Frequency (RF) tags attached or positioned close to the vibrating target object can be efficiently utilized to introduce an extra modulating effect in the coherent vibration sensing scenario and to improve the sensing performance. For example, RF harmonic tags [20] and UHF RFID tags [21] which respectively consists a non-linear and a modulating electronic component can be applied to enhance the vibration sensing performance. This idea has been presented in 2012

The authors are with the University of Grenoble Alpes, Grenoble INP, LCIS, F-26000 Valence, France (email: ashkan.azarfar@lcis.grenoble-inp.fr).

by [22] where an RF harmonic tag is employed to provide a perfect environment clutter rejection and to robustly sense the human respiration at the distance of 1 m using a harmonic coherent Doppler radar working at the low carrier frequency of 2.45 GHz. With the same approach as [22], harmonic UHF RFID tags have been used in [23] for vibration sensing while the identification capability is also included compared to [22].

The Near-field Coherent Sensing (NCS) approach has been demonstrated in [24] for vital sign monitoring. Basically in [24], a harmonic RFID tag is positioned close to the body chest and the movement caused by the heart beat produces a varying near-field boundary for the tag antenna which its radiation is strongly coupled into the body. This time-varying near-field boundary change is modeled as a load modulation for the tag antenna which can be retrieved from the amplitude-modulated backscatter wave with a coherent reader. The most important point in the approach proposed by [24] is that with a very low carrier frequency of 950 MHz and a vibration amplitude less than 1 mm (heart beat motion), the significant modulation contribution is due to the near-field changing effect while the Doppler (phase) modulation produced by this vibration is quite small at this frequency and it is very hard to be detected. The idea in [24] has been applied later for sleep scoring in [25] and for vocal cord vibration sensing in [26]. However, in all the approaches presented by [22]–[26], the utilized RF tags include an electronic component which increases the tag structure complexity and its fabrication cost, and also arises some environmental issues for the large scale usage of the tags. It is why, in-contact microwave sensors composed of passive resonators which do not include any electronic component have been used in [27] and [28] to respectively detect the throat vibration and fingertip pulse based on the near-field modulation (similar to the concept of the NCS in [24]). However, the in-contact passive sensors presented by [27], [28] need to be positioned tightly in contact with the human body and to be measured using costly physical connections which no longer allows remote retrieval of data.

The chipless RFID technology [29]–[31] has been mainly introduced to reduce the tag fabrication cost compared to classical UHF RFID, whereas the reading range of the chipless RFID tags ($\approx$ 30 cm) is much smaller than that of classical UHF chipped RFID tags (several meters) due to the Linear Time-Invariant (LTI) properties of the chipless tags [32]. Chipless technology has been employed in different sensing applications such as movement sensing [33], [34], temperature sensing [35], [36], humidity sensing [37], and electric permittivity sensing [38], [39] while the sensing range in all these works is limited by 50 cm. Recently in [40]–[42], it has been demonstrated that moving chipless tags can be detected in large distances (up to several meters) with the Doppler modulation which breaks the LTI property for chipless tags. It should be mentioned that, same as [4]–[19], the Doppler effect is the only considered motion-induced modulation source in [41], [42]. However, an extra motion-induced modulating effect (as the near-field boundary variation) can be always implemented in the chipless tag design. Using this idea, the modulation efficiency of the moving chipless tags can be enhanced significantly compared to pure Doppler-modulated chipless tags presented in [41], [42].

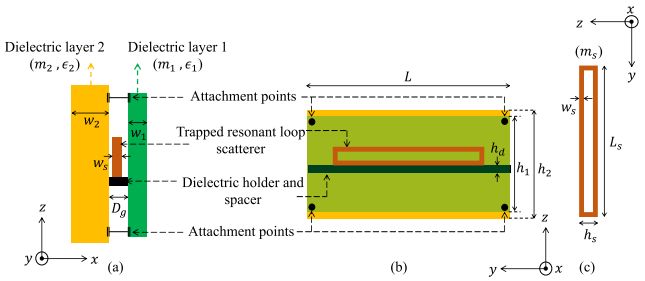

Fig. 1. Structure of the proposed multi-state chipless tag. (a) Side view. (b) Front view. (c) Rectangular wire loop scatterer.

In this paper, we propose motion-modulated multi-state chipless RFID tags for vibration sensing which provide a near-field boundary modulation in addition to the Doppler modulation when they are attached to a vibrating object. This concept is used to detect the vibration much more effectively compared to when only the Doppler modulation is produced by the vibration. The proposed approach can be applied for robust vibration sensing in large distances while the target object can be also identified. The paper is organized as follows. Section II presents the structure of the multi-state chipless tag and introduces the developed multi-physics model for backscattering from the tag during vibration. Section III describes the tag implementation and the measurement bench, and discusses the experimental results in terms of sensing range and robustness. Finally, Section IV concludes the paper.

II. Principle of Operation and Model

A. Multi-state chipless tag structure

The structure of the proposed multi-state chipless tag which provides a near-field boundary modulation as it vibrates, is shown in Fig. 1. Basically, as it is shown in Fig. 1 (a) and (b), the chipless tag is composed of a rectangular loop wire resonant scatterer which is trapped in between of the two dielectric layers. The length, the height, and the mass of the rectangular wire loop are respectively L_s, h_s, and m_s while the diameter of the wire (which is equal to the thickness of the loop) is w_s [Fig. 1 (c)]. The two dielectric layers DL1 and DL2 are formed as two rectangular slabs with the length of L and the respective heights of h_1 and h_2 and they are attached to each other at four vertices attachment points such that the gap distance between them is tightly fixed by a dielectric holder and spacer with the thickness of D_g and the height of h_d. The two dielectric slabs DL1 and DL2 have respectively a thickness of w_1 and w_2, a relative permittivity of ϵ_{r1} and ϵ_{r2}, and a mass of m_1 and m_2. The thickness of the loop w_s and the gap distance D_g is considered such that the loop scatterer can freely move in between the two dielectric layers ($D_g > w_s$).

B. Mechanical Model

We assume that the multi-state chipless tag is vibrating along x-axis and it is positioned parallel to the gravity direction (z-axis) as shown in Fig. 2 (a). The amplitude and

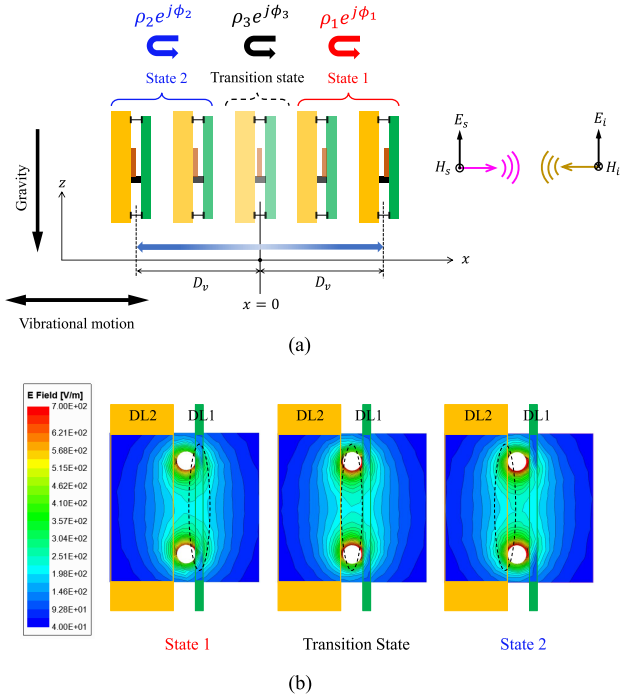

Fig. 2. (a) Backscattering from the vibrating multi-state chipless tag. (b) Distribution of the electric field over the cross-section of the multi-state chipless tag simulated at the three resonance frequencies associated with each state where the field confined region is shown with the dashed ellipse.

angular frequency of the vibration is respectively D_v (with $D_v > D_g$) and ω_v. In this configuration, the dielectric holder of the tag keeps the loop scatterer in between the two dielectric layers and prevents the loop to fall down. Moreover, the loop scatterer can have a free but bounded motion between the two dielectric layers along x-axis since $D_g > w_s$. In fact, due the vibrational motion of the tag, the loop is bouncing between the surfaces of the two dielectric layers. From physical point of view, when the tag is attached to a vibrating object, since naturally the mass of the vibrating object m_o (e.g. human body or a mechanical structure) is much greater than the one of the tag ($m_o \gg m_1 + m_2 + m_s$), to analyze the bounded motion of the loop, the friction force between the loop and the holder can be neglected compared to the force that caused the vibration. Consequently, the bouncing motion of the loop during the vibration of the tag can be modeled by considering the multiple collisions of the loop with the two dielectric layers while it is not affected by the friction and the gravity forces. For the assumed single tone vibration, the position of the left surface of DL1 [$x_1(t)$] and the right surface of DL2 [$x_2(t)$] when the loop is bouncing between them can be written in time as

$$\begin{cases} x_1(t) = -\dfrac{D_g}{2} + D_v \sin\omega_v t & \text{(1a)} \\ x_2(t) = \dfrac{D_g}{2} + D_v \sin\omega_v t & \text{(1b)} \end{cases}$$

To analyze the multiple collisions of the loop, it is assumed that $m_s \ll m_1 + m_2 = m_b$ (where m_b is the total mass of the tag body: the two connected dielectric layers) and the collision of the loop and the dielectric layers is elastic, which can be

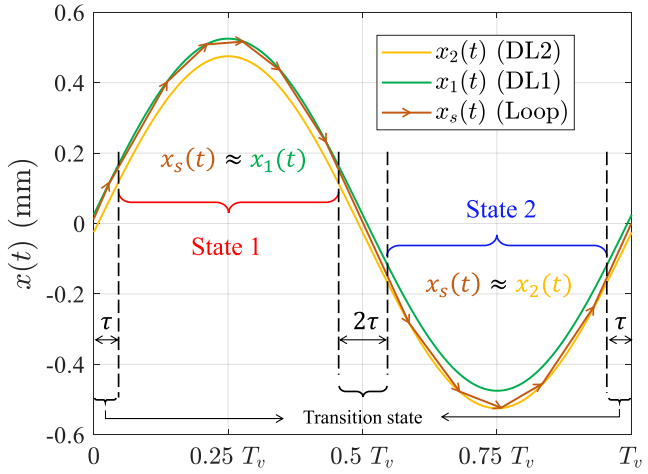

Fig. 3. Calculated steady state bouncing trajectory of the trapped loop scatterer between the two vibrating dielectric layers during one vibration period.

briefly expressed in terms of momentum and kinetic energy conservation equations as

$$\begin{cases} m_s v_s^- + m_b v_b^- = m_s v_s^+ + m_b v_b^+ & \text{(2a)} \\ \dfrac{1}{2} m_s (v_s^-)^2 + \dfrac{1}{2} m_b (v_b^-)^2 = \dfrac{1}{2} m_s (v_s^+)^2 + \dfrac{1}{2} m_b (v_b^+)^2 & \text{(2b)} \end{cases}$$

where v_s^- and v_s^+ are the velocity of the loop respectively before and after each collision, and v_b^- and v_b^+ are those of the tag body. It should be mentioned that (2) is identically applied for the both collisions on the left and right side surfaces since the two dielectric layers are tightly connected. The motion trajectory of the bouncing loop between the two dielectric layers during the vibration of the tag can be obtained using a successive numerical solution based on (1) and (2). For example, for $D_v = 0.5$ mm, $D_g - w_s = 0.05$ mm, and $m_b = 100\, m_s$, the steady state bouncing trajectory of the loop $x_s(t)$ is shown in Fig. 3 for one period of vibration $T_v = 2\pi/\omega_v$. The parametric study of the problem results in the fact that, regardless of the vibration frequency $f_v = 1/T_v$, for $D_v \gg (D_g - w_s)$, the steady state bouncing trajectory of the loop during each period of vibration can be divided into three intervals with associated states as: the 'State 1 (S1)' for the interval $q_1 = [\tau\,,\, T_v/2 - \tau]$ in which the loop scatterer is almost in touch with DL1 , the 'State 2 (S2)' for the interval $q_2 = [T_v/2 + \tau\,,\, T_v - \tau]$ in which the loop scatterer is almost in touch with DL2, and the 'Transition State (TS)' for the interval $q_3 = [0\,,\, T_v] - (q_1 \cup q_2)$ in which the loop scatterer is somewhere between DL1 and DL2, as it is illustrated in Fig. 3. However, the S1 and the S2 cover the main portion of the vibration period (almost the first half-cycle in S1 and almost the second half-cycle in S2) while the TS covers less than 10% of the vibration period which means $\tau < T_v/10$. Accordingly, the steady state bouncing trajectory of the loop $x_s(t)$ can be approximated for each vibration period as

$$\begin{cases} x_s(t) = x_1(t) \quad t \in q_1 \quad \text{(S1)} & \text{(3a)} \\ x_s(t) = x_2(t) \quad t \in q_2 \quad \text{(S2)} & \text{(3b)} \\ x_2(t) < x_s(t) < x_1(t) \quad t \in q_3 \quad \text{(TS)} & \text{(3c)} \end{cases}$$

TABLE I
CHARACTERISTICS OF THE DESIGNED MULTI-STATE CHIPLESS TAG

w_1	0.2 mm	w_s	0.4 mm
w_2	8 mm	h_s	2.5 mm
ϵ_{r1}	2.4	L_s	30 mm
ϵ_{r2}	1.3	D_g	0.45 mm
$h_1 = h_2$	60 mm	L	60 mm

which can be used to model the problem in term of electromagnetic behaviour. Worth mentioning that, since the position of the loop scatterer with respect to the two dielectric layers changes during vibration (the three states for the tag structure), the proposed chipless tag is called 'Multi-State (M-S)' tag, whereas for the specific case of $D_g = w_s$, the presented chipless tag behaves like classical chipless tags that their structure does not change during the vibration, and so it is called 'Single-State (S-S)' tag.

C. Backscattering form vibrating multi-state chipless tag

Fig. 2 (a) illustrates the vibrating M-S chipless tag impinged by a vertically polarized (z-polarized) plane electromagnetic wave at the frequency f_0 which can be expressed as

$$\vec{E}_i(\vec{r}) = E_0\, e^{jkx}\, \hat{z} \tag{4}$$

where $k = 2\pi/\lambda$, $\lambda = c_0/f_0$, and c_0 is the free space light velocity. Generally, for the rectangular loop scatterer with $h_s \ll L_s$ which is located in the free space and its smaller side is aligned with the z-axis, the fundamental resonant mode of the loop is perfectly excited by the incident z-polarized wave when $L_s = \lambda/2$. However, since the rectangular loop is sandwiched between the two dielectric layers in the proposed M-S chipless tag, the near-field boundary condition of the loop scatterer is significantly affected by the two dielectric layers and their characteristics as thicknesses (w_1, w_2), relative permittivities (ϵ_{r1}, ϵ_{r2}), and the gap distance between the loop and the layers ($D_g - w_s$). So, the status of the M-S chipless tag (S1, S2, or TS) has an effect on the near-field distribution of the loop scatterer. Definitely, this near-field boundary variation between different states of the tag will change the resonance frequency of the fundamental mode of the loop scatterer, and consequently, modifies the scattering parameters of the chipless tag. To demonstrate this fact using numerical study, a M-S chipless tag with the characteristics noted in Table I is simulated by CST Microwave Studio. With the configuration shown in Fig. 2 (a), the M-S chipless tag is simulated while it is assumed stationary in the three states (S1, S2, and TS) and impinged by the z-polarized plane wave. It should be mentioned that, in the transition state (TS), without lacking generality, the loop is positioned exactly in the middle of the two dielectric slabs in the simulation. The tag is impinged by the z-polarized plane wave (4) with $4.2 < f_0 < 4.35$ GHz and $E_0 = 1$ V/m, and the z-polarized backscattered wave generated by the fundamental resonant mode of the loop scatterer is calculated by simulation. Accordingly, the vertical scattering parameter of the M-S chipless tag $S_{vv}(f_0)$ is obtained for

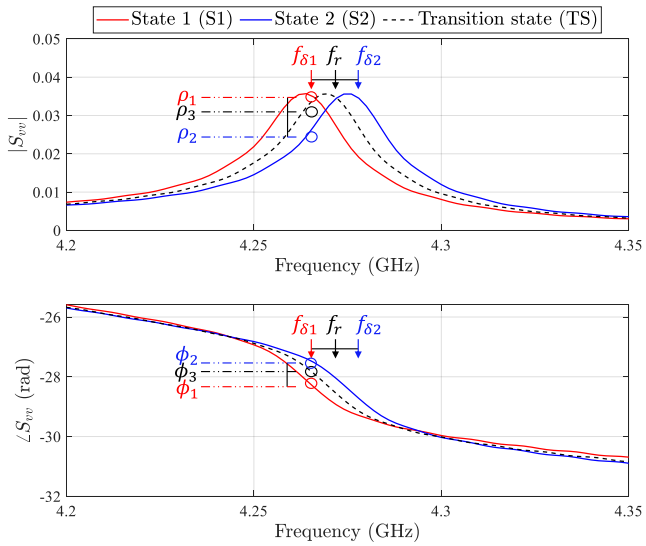

Fig. 4. Magnitude and phase of the vertical scattering coefficient S_{vv} as a function of frequency simulated at the three states of the M-S chipless tag.

the three states as it is shown in Fig. 4, while the resonance frequency of the tag in the S1, S2, and the TS is respectively $f_{\delta 1} = 4.264$ GHz, $f_{\delta 2} = 4.276$ GHz, and $f_r = 4.270$ GHz. The cross-section view of the electric field distribution around the loop scatterer (in a 4×4 mm square area of the tag cross-section) is given in Fig. 2 (b) at the associated resonance frequencies of the three states of the tag. As it can be observed in Fig. 2 (b), although the considered gap between the loop and the two dielectric layers ($D_g - w_s = 0.05$ mm) is very small compared to the wavelength [$(D_g - w_s)/\lambda \approx 7 \times 10^{-4}$], the near-field distribution of the loop scatterer is relatively modified for the three different states of the tag such that the electric field of the fundamental mode in S1 and S2 is respectively more coupled to DL1 and DL2, while in TS the field is mostly confined in between the two dielectric layers. This near-field variation caused by the very small gap is translated to a significant variation of the scattering response of the tag in different states. This is the key idea of the paper that how this slight near-field modulation in M-S chipless tags can efficiently improve the modulation capability of the tag when it moves.

The backscattered field from the vibrating M-S chipless tag can be analytically formulated based on the simulation results obtained for the three states of the tag shown in Fig. 4 and the trajectory of the tag shown in Fig. 3. For the incident plane wave at f_0, the complex scattering coefficient of the tag $S_{vv}(f_0)$ in the three states S1, S2, and TS is respectively considered as $\rho_1\, e^{j\phi_1}$, $\rho_2\, e^{j\phi_2}$, and $\rho_3\, e^{j\phi_3}$ (for example, the scattering coefficient in each state is shown in Fig. 4 for $f_0 = f_{\delta_1}$). Worth mentioning that, for $(D_g - w_s)/\lambda \ll 1$ which causes the near-field of the loop scatterer to be strongly coupled into the two dielectric layers, regardless of where exactly the loop is located in between the two dielectric layers (at the middle [corresponds to the simulation result shown in Fig. 4] or at anywhere in between), the resonance frequency of the tag in TS is always bounded between the resonance

frequency of the tag in S1 and S2 ($f_{\delta 1} < f_r < f_{\delta 2}$). As it is shown in Fig. 2 (a), considering both vibration-induced modulations (the near-field boundary modulation and the natural Doppler modulation), the periodic time-varying complex envelope of the backscattered field $\vec{E}_s(r,t)$ from the vibrating M-S chipless tag can be expressed in each period of vibration as

$$\vec{E}_s(r,t) = \hat{z}E_0\frac{e^{-jkr}}{r} \times \begin{cases} \rho_1 e^{jk\phi_1} e^{j\beta\sin(\omega_v t)} & t \in q_1 \\ \rho_2 e^{jk\phi_2} e^{j\beta\sin(\omega_v t)} & t \in q_2 \\ \rho_3 e^{jk\phi_3} e^{j\beta\sin(\omega_v t)} & t \in q_3 \end{cases} \quad (5)$$

where $\beta = 4\pi D_v/\lambda$ is the Doppler modulation index. In fact in (5), the three different scattering coefficients ($\rho_1\, e^{j\phi_1}$, $\rho_2\, e^{j\phi_2}$, and $\rho_3\, e^{j\phi_3}$) associated with the three states of the chipless tag (S1, S2, and TS) are considered in the corresponding time interval (q_1, q_2, and q_3) in each vibration period, which imposes a quasi-digital amplitude-phase modulation on the backscattered wave. In addition, a continuous sinusoidal phase (Doppler) modulation due to the vibrational movement of the tag is considered on the backscattered wave expressed in (5). It should be mentioned that, the result obtained in (5) can be also calculated using a sequence of frequency-domain simulations in which the position and the status of the chipless tag is changed at each step according to (1) and (3). This approach is called "frozen-time" solution based on quasi-stationary approximation [43]. The results obtained by frozen-time simulations (as a reference solution) and the analytical expression in (5) are compared in the following.

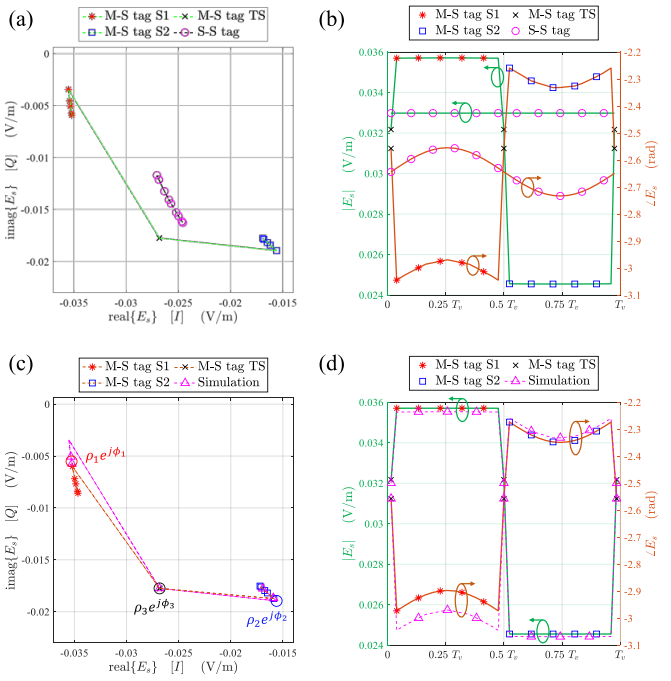

Fig. 5. (a) I/Q diagram and (b) magnitude/phase profile of the modulated backscattered field from the vibrating M-S (at $f_0 = f_{\delta 1}$) and S-S (at the resonance $f_0 = 4.269$ GHz) chipless tag obtained by frozen-time simulations. (c) I/Q diagram and (d) magnitude/phase profile of the backscattered field form the vibrating M-S chipless tag at $f_0 = f_{\delta 1}$ calculated based on (5) with simulated stationary scattering coefficients shown in Fig. 4. The simulation results for the M-S and S-S chipless tag shown in (a) and (b) are superimposed in (c) and (d) for comparison.

D. Time and frequency domain analysis

To clearly demonstrate how the backscattered wave is modulated by the vibrating M-S chipless tag, the backscattered field is studied in time and frequency domain. The time-domain variation of the modulated backscattered field calculated by the frozen-time simulation is presented in Fig. 5 (a) and (b) respectively in terms of In-phase/Quadrature (I/Q) components and magnitude/phase profiles. The simulation is done for the vibrating M-S chipless tag with the characteristics noted in Table I at the frequency $f_0 = f_{\delta 1} = 4.264$ GHz while $D_v = 0.5$ mm and the field monitor is located at 1 m distance from the tag in CST setup. The I/Q diagram shown in Fig. 5 (a) displays the fact that the modulation induced by the vibrating chipless tag can be considered as a multi-state modulation (like what is basically implemented in chipped UHF RFID with two states [21]) in which the modulated signal is mostly concentrated around two points in the I/Q plane associated with the two main states of the chipless tag (S1 and S2), while the small variation of the signal around S1 and S2 is caused by the vibration-induced phase (Doppler) modulation. In addition, the phase and magnitude variation of the backscattered field is presented in Fig. 5 (b) during one period of vibration showing that both the magnitude and phase profiles drastically change at the transition state. However, at the two main states (S1 and S2) of the tag, the magnitude of the backscattered wave remains constant and the partially sinusoidal phase variation is observed due to the Doppler modulation. Moreover, the I/Q diagram and magnitude/phase profile of backscattered field from the vibrating M-S chipless tag at $f_0 = f_{\delta 1}$ is compared with those of the vibrating S-S chipless tag (which corresponds to the specific case of $D_g = w_s$ with the same $D_v = 0.5$ mm) at its resonance frequency ($f_0 = 4.269$ GHz) respectively in Fig. 5 (a) and (b). As it can be observed, the vibrating S-S tag has the classical circular arc I/Q path which is associated with the constant magnitude and the sinusoidal phase variation. Obviously, the vibrating M-S chipless tag provides a much longer I/Q path compared to the vibrating S-S tag which shows the vibrating M-S chipless tag can more efficiently modulate the backscattered wave. Finally, Fig. 5 (c) and (d) respectively show the I/Q diagram and the magnitude/phase profile of the backscattered field from the M-S chipless tag which is analytically calculated using (5) with $\rho_i\, e^{j\phi_i}\,; i = 1,2,3$ obtained from the simulation results shown in Fig. 4 (a) and (b) at $f_0 = f_{\delta 1}$. The analytically calculated results are in good agreement with those obtained by simulation and consequently prove the validity of (5).

Besides the time domain analysis, considering the imposed modulation by the vibrating M-S chipless tag in the frequency domain will provide a good insight about the exact behaviour of the proposed backscatter modulation technique. Since the modulated backscattered field in (5) is a periodic function with the same period as the vibration, it can be expressed in term

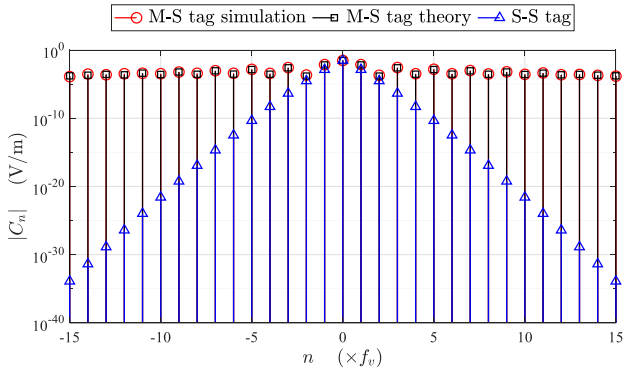

Fig. 6. Calculated Fourier coefficients of modulated backscattered field from the vibrating M-S and S-S chipless tag. Calculations have been done based on frozen-time simulations and the analytical expression in (5).

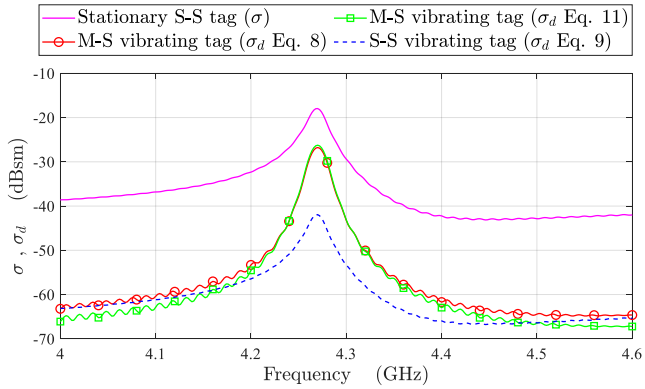

Fig. 7. Calculated differential RCS of the vibrating M-S and S-S chipless tag. The stationary RCS of the S-S chipless tag is superimposed for comparison.

of Fourier expansion as

$$\vec{E}_s(r,t) = E_0 \frac{e^{-jkr}}{r}\hat{z} \sum_{n=-\infty}^{+\infty} C_n e^{jn\omega_v t} \tag{6}$$

where C_n is the Fourier coefficients of the modulated backscattered field, which can be obtained based on the simulation results and also based on (5). Accordingly, the frequency representation of the backscattered field can be written as

$$\vec{\mathbf{E}}_s(r,f) = E_0 \frac{e^{-jkr}}{r}\hat{z} \sum_{n=-\infty}^{+\infty} C_n\, \delta(f - nf_v) \tag{7}$$

The magnitude of the calculated C_n for the backscattered wave from the vibrating M-S tag at $f_0 = f_{\delta 1} = 4.264$ GHz and the S-S chipless tag at $f_0 = 4.269$ GHz are presented in Fig. 6. It is obviously illustrated in Fig. 6 that the level of the modulated harmonics at nf_v, $n \neq 0$ are much higher (especially for $|n| > 2$) for the vibrating M-S tag in comparison with the S-S tag, which results in a larger modulated backscattered power as it was predicted.

It should be mentioned that in all the above-presented results, the position of the loop scatterer is considered exactly at the middle of the two dielectric layers during the transition state ($x_s(t) = [x_1(t) + x_2(t)]/2 \;;\; t \in q_3$), while it does not affect the general validity of the obtained results since the position of the loop in TS just change the $\rho_3\, e^{j\phi_3}$ point through which the signal pass for a very small portion of the vibration period.

E. Differential RCS

The concept of differential RCS (delta RCS or σ_d) has been originally introduced for chipped UHF RFID tags where the differential RCS of a tag is calculated based on the two chip impedance states [44]. Recently in [45], the concept of differential RCS has been generalized for all the modulating tags based on a frequency-domain analysis. Essentially, the differential RCS is a range-independent parameter [exactly like the classical RCS (σ)] which perfectly shows how much a modulating tag (tag with any kind of time-varying property) can efficiently modulate the backscattered wave, and accordingly, the read range of the tag can be estimated based on the measured differential RCS using the radar equation. Assuming that the modulating tag is excited at a definite carrier frequency, the σ_d in [45] is directly related to the total power carried by the modulated frequency components around the carrier in the backscattered signal. According to [45], the differential RCS of the vibrating M-S chipless tag at f_0 can be calculated based on (7) and expressed as

$$\sigma_d^{\text{M-S}}(f_0) = \lim_{r\to\infty} 4\pi r^2 \frac{\int_B |\vec{\mathbf{E}}_s(r,f)|^2\, df}{|E_0|^2} = 4\pi \sum_{\substack{n=-\infty \\ n\neq 0}}^{+\infty} |C_n|^2 \tag{8}$$

where $B = (-\infty, 0^-] \cup [0^+, +\infty)$ is the zero-excluded integration interval removing the unmodulated portion of the backscattered power located at f_0. Using the same calculation method in [41], the differential RCS of a vibrating S-S (classical) chipless tag with a RCS of $\sigma(f_0)$ has been obtained as

$$\sigma_d^{\text{S-S}}(f_0) = \sigma(f_0)(1 - [J_0(\beta)]^2) \tag{9}$$

where $J_0(\beta)$ is the zero-order first kind Bessel function and β is the Doppler modulation index. The calculated differential RCS of the vibrating M-S chipless tag based on (8) and that of the vibrating S-S chipless tag based on (9) are shown in Fig. 7. The RCS of the stationary S-S chipless tag simulated with CST is also plotted to have an idea about the maximum achievable differential RCS. The differential RCS of the vibrating M-S chipless tag is maximized at $f_0 = 4.271$ GHz located between $f_{\delta 1}$ and $f_{\delta 2}$ (the resonance frequencies of the tag in the two main states S1 and S2) which is very close to the resonance frequency of the tag in the transition state ($f_r = 4.270$ GHz). Note that since the considered gap in the M-S chipless tag is very small ($Dg - w_s = 0.05$ mm), the resonance frequency of the S-S chipless tag ($D_g = w_s$) is also quite close to the $f_r = 4.270$ GHz. The important result shown in Fig. 7 is that the maximum differential RCS of the vibrating M-S chipless tag is significantly higher (> 15 dB) than that of the vibrating S-S tag, which theoretically verifies the main idea of the paper in term of differential RCS enhancement based on motion-induced near-field modulation. The great improvement achieved in differential RCS by using the M-S chipless tag

definitely leads to enlarging the vibration sensing range and increasing the sensing robustness in real scenarios.

Although the differential RCS of the vibrating M-S chipless tag is calculated based on the general formula in (8), it is very important to analytically express the differential RCS in terms of the stationary scattering parameters of the tag, like what has been done for vibrating classical (S-S) chipless tags in (9) [41]. This kind of analytical expression can be efficiently used to predict the resultant differential RCS based on stationary parameters. Since it has been clearly shown that the contribution of the Doppler modulation is negligible compared to the near-field boundary modulation for the vibrating M-S chipless tag (Fig. 7), it is logical to suppress the vibration-induced phase (Doppler) modulation terms in (5), and to approximate the backscattered field in each state with a time-independent state value, which yields a real multi-state transponder model for the vibrating chipless tag expressed by a stochastic process as

$$\vec{E}_s(r,t) = \hat{z}E_0\frac{e^{-jkr}}{r} \times \begin{cases} \rho_1\, e^{j\phi_1} & p = p_1 \\ \rho_2\, e^{j\phi_2} & p = p_2 \\ \rho_3\, e^{j\phi_3} & p = p_3 \end{cases} \tag{10}$$

where p_1, p_2, and p_3 are the respective probability assigned to the field state values at S1, S2, and TS. These probabilities can be defined based on the time portion during which the tag remains in each state in one period of vibration. Accordingly, they can be considered as $p_1 = 0.46$, $p_2 = 0.46$, and $p_3 = 0.08$ while the transition state is assumed to be passed such quickly that its associated probability is less than 0.1. Based on the approach presented in [46], the analytical expression of σ_d^{MS} for the vibrating M-S chipless tag is derived in terms of stationary scattering coefficients associated to each state as

$$\sigma_d^{\text{M-S}}(f_0) = 4\pi \sum_{i=1}^{3} p_i |\rho_i\, e^{j\phi_i} - \bar{\rho}|^2 \tag{11}$$

where $\bar{\rho} = \sum_{i=1}^{3} p_i\, \rho_i\, e^{j\phi_i}$ is the expectation of the scattering coefficients. The calculated differential RCS of the vibrating M-S chipless tag based on the analytical expression in (11) is also presented in Fig. 7 which is perfectly in accord with the results obtained using (8). This fact proves the validity of (11) and demonstrates that the proposed chipless tag can be accurately modeled as a multi-state modulating transponder when it vibrates, while the involved modulation significantly increase the differential RCS of the vibrating chipless tag.

III. Results and Discussion

A. Tags implementation

Fig. 8 (a) and (b) respectively show the implemented prototype of the M-S chipless tag and the S-S chipless tag. Both tags are implemented on a single rectangular 8×10 cm piece of foam sheet (foam support) which will be attached to a loudspeaker to realize the vibration. Note that the design characteristics of the M-S chipless tag used for the simulation indicated in Table I have been selected based on the fabricated prototype. For the M-S chipless tag, a rectangular copper-wire loop with $L_s = 28.5$ mm, $h_s = 2.6$ mm, and $w_s = 0.4$ mm is created and it is trapped between a 4×4 cm polyester

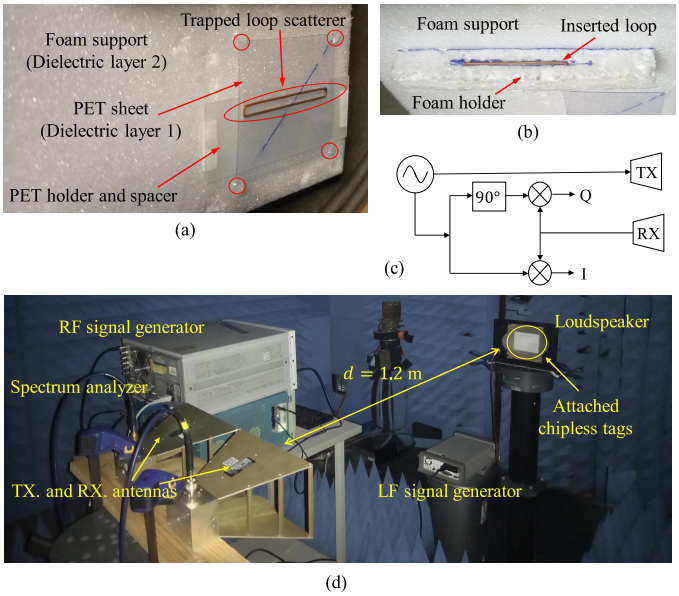

Fig. 8. Fabricated prototype of the (a) M-S and (b) S-S chipless tag. (c) Architecture of the classical coherent IQ transceiver. (d) Measurement bench used for vibration sensing in the anechoic chamber.

(PET) sheet with $w_1 = 0.2$ mm and $\epsilon_{r1} \approx 2.4$, and the foam support with $w_2 = 8$ mm and $\epsilon_{r2} \approx 1.3$. As it is indicated in Fig. 8 (a), the PET sheet is DL1 and the foam support is DL2. The PET sheet (DL1) is attached to the foam support (DL2) using silicon glue at the four vertices points as it is shown by four red circles in Fig. 8 (a). In the meantime, a PET holder and spacer with the thickness of $D_g = 0.5$ mm and $h_d = 1.9$ cm has been tightly sandwiched between the PET sheet and the foam support. The PET spacer will fix the gap distance between DL1 and DL2, while it will also hold fixed the orientation and position of the loop scatterer as shown by the red ellipse in Fig. 8 (a). Thus, the M-S chipless tag has been implemented according to the proposed structure in Fig. 1 with $D_g - w_s \approx 0.1$ mm. However, due to the limitations of the fabrication process it was not possible to realize the S-S chipless tag with the same case as in the simulation to put $D_g = w_s$. In fact, to do that the PET spacer should be removed to make the loop tightly sandwiched between the PET sheet and the foam support. Nevertheless, because of the flexibility of the PET sheet, an undesired gap is still remained which breaks the required condition for S-S chipless tag. Consequently, the S-S chipless tag is realized in a different way as shown in Fig. 8 (b). Actually, to avoid any gap in the structure of the S-S chipless tag with the same rectangular loop scatterer, a super narrow slot is cut by blade through a spongy foam holder and the loop is firmly inserted into the foam holder as it is illustrated in Fig. 8 (b). The spongy foam holder is glued to the same foam support on which the M-S chipless tag has been realized, and the foam support is attached to a loudspeaker in the measurement bench. It should be mentioned that, although the structure and the used dielectrics for the implemented M-S and S-S chipless tag are different, the resonance frequency of the tags will also be different. Despite this, as the dielectric loss of all used

materials (foam, PET, and spongy foam) are negligible, the stationary RCS of both realized tags is almost identical.

B. Measurement bench in anechoic chamber

Similar to all vibration sensing methods based on coherent microwave interferometry, the vibrating multi-state chipless tag also can be measured using the classical coherent IQ transceiver with the architecture shown in Fig. 8 (c) where a single microwave oscillator is employed for both transmitting (TX) and receiving (RX) part to perfectly satisfy the coherency. However, in this work, the coherent IQ transceiver is realized using an RF signal generator (HP 8720D) and a spectrum analyzer (Tektronix RSA3408A) while their internal oscillators are synchronized using a common 10 MHz reference signal. The measurement bench used for the experimental study in the anechoic chamber is presented in Fig. 8 (d). The bench is composed of the signal generator and the spectrum analyzer which are respectively connected to the TX and RX antennas (A.H. Systems SAS-571) both configured in vertical polarization. The vibration is realized using a loudspeaker which is mounted vertically on a stand as shown in Fig. 8 (d). In this configuration, the diaphragm of the speaker vibrates horizontally (parallel to the ground surface and perpendicular to the gravity direction) and the foam support of the fabricated tags is attached to the diaphragm such that the larger side of the loop is aligned horizontally. Consequently, the implemented condition for the vibrating M-S chipless tag is compatible with the presented mechanical model. The loudspeaker is fed by a low-frequency (LF) signal generator shown in Fig. 8 (d) providing the sinusoidal voltage signal as $V_m \sin 2\pi f_v t$ which cause the loudspeaker to produce a single tone vibration. Due to the non-uniform frequency response of the loudspeaker, to produce the maximum range for the vibration amplitude, the vibration frequency is set at $f_v = 58$ Hz where the diaphragm mechanically resonates. Worth mentioning that, since from mechanical point of view the functionality of the presented method is independent of the vibration frequency, the specific choice for f_v does not affect the experimental proof of concept. The amplitude of the voltage fed to the speaker is set $V_m = 2.5$ V while the corresponding vibration amplitude is measured as $D_v = 0.48$ mm [41] which is close to what has been used in simulations. The loudspeaker is positioned at $d = 1.2$ m distance from the antennas to fulfill the far-field radiation condition. The RF signal source generates stepped CW carriers at $f_0 = 4.5 : 0.01 : 5.3$ GHz with the power of $P_t = 0$ dBm while the spectrum analyzer captures the reflected signal in a $BW = 1$ kHz span around each carrier.

C. Vibration sensing performance

The performance of the M-S and S-S chipless tags in vibration sensing is examined based on the measured differential RCS of each tag. According to (8), the differential RCS of the vibrating chipless tags can be calculated based on the Power Spectral Density (PSD) of the backscattered signal $S_r(f)$ measured by the spectrum analyzer. Thus, the differential part

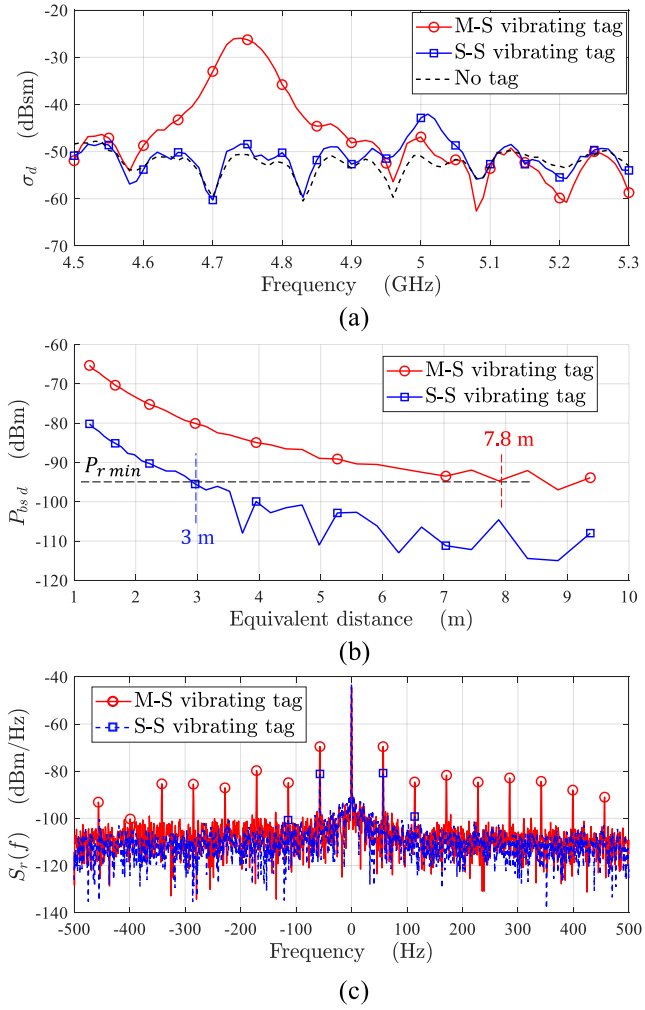

Fig. 9. (a) Measured differential RCS of the vibrating M-S and S-S chipless tags as a function of carrier frequency f_0. The case 'No tag' is for when the loop scatterer is not present on the loudspeaker. (b) Differential backscattered power from S-S and M-S vibrating chipless tag as a function of sensing distance. (c) Measured PSD of the modulated backscattered signal from the vibrating M-S and S-S chipless tag at their respective resonance frequencies.

(modulated part) of the backscattered power $P_{bs\,d}$ at the carrier f_0 is obtained as

$$P_{bs\,d}(f_0) = \int_{-BW/2}^{-\epsilon_m} S_r(f)\,df + \int_{+\epsilon_m}^{+BW/2} S_r(f)\,df \qquad (12)$$

where $2\epsilon_m$ is the minimal bandwidth which allows to remove the power at $f = 0$ Hz ($f = 0$ Hz corresponds to the f_0 after down-conversion in the spectrum analyzer). Based on the well-known radar equation, the measured differential RCS at f_0 can be expressed as

$$\sigma_d(f_0) = \frac{(4\pi)^3 d^4 P_{bs\,d}(f_0)}{\lambda^2 G_r G_t (1-|\Gamma_r|^2)(1-|\Gamma_t|^2) P_t} \qquad (13)$$

where G_r , Γ_r and G_t , Γ_t are respectively the gain and the input reflection coefficient of the receiving and the transmitting antennas. The measured differential RCS of the vibrating loudspeaker calculated using (12) and (13) is presented in Fig. 9 (a) as a function of carrier frequency f_0 for the three

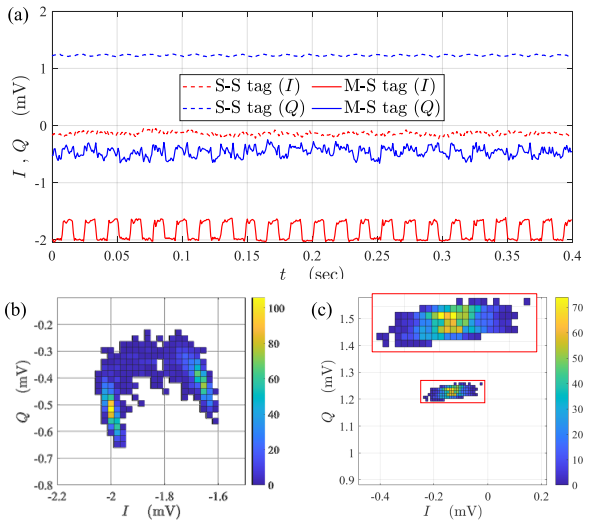

Fig. 10. (a) Measured raw I/Q components of the backscattered signal from the vibrating M-S and S-S chipless tag as a function of time. Two-dimensional time histogram of the measured I/Q data samples in the I-Q plane for the vibrating (b) M-S and (c) S-S chipless tag. The scale and the length of the I/Q axes are identically set for plots in (b) and (c).

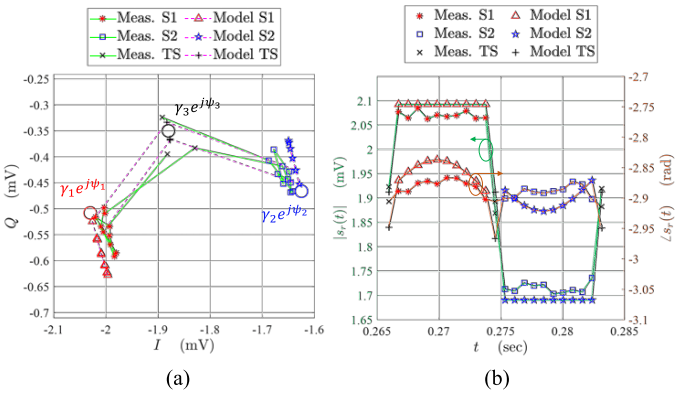

Fig. 11. (a) Measured I/Q diagram and (b) measured magnitude/phase profile of the modulated backscattered signal from the vibrating M-S chipless tag at the resonance frequency associated with the maximum differential RCS. The calculated I/Q path and magnitude/phase profile based on the model are added for comparison.

cases: 1) the loop scatterer is configured in the M-S tag on the foam support, 2) the loop scatterer is configured in the S-S tag on the foam support, and 3) the loop scatterer is not present on the foam support ('No tag'). The resonance associated to the M-S ($f_0 = 4.74$ GHz) and the S-S ($f_0 = 5.01$ GHz) vibrating chipless tag is clearly recognized in terms of differential RCS as it is shown in Fig. 9 (a), while no resonance is observed for the 'No tag' case. As previously explained, the difference between the resonance frequencies of the M-S and S-S chipless tags is natural due to the fact that they have not been realized with the same structure (the used dielectrics). The most important result illustrated in Fig. 9 (a) is that the maximum level of the differential RCS obtained by the M-S chipless tag is almost 15 dB higher than that obtained by the S-S tag, which is perfectly in agreement with what was predicted based on the analytical and simulation results shown in Fig. 7. The observed resonance in the differential RCS profiles of both vibrating tags (M-S and S-S) demonstrates the identification capability for the vibrating chipless tag. However, obviously, the maximum detection range for the M-S chipless tag will be significantly larger than that of the S-S chipless tag, while the vibration amplitude is the same for both tags. This fact has been experimentally verified by measuring the differential backscattered power $P_{bs\,d}$ from both S-S and M-S vibrating chipless tags in their respective resonance frequency while the transmitted power P_t has been decreased, which is equivalent to increasing the sensing distance. By decreasing P_t from 0 dBm to -30 dBm at the fixed distance of $d = 1.2$ m, the equivalent increasing distance can be calculated using the radar equation, and consequently, the measured $P_{bs\,d}$ is obtained as a function of equivalent distance as it is shown in Fig. 9 (b). By considering the sensitivity of the receiver at $P_{r\,min} = -95$ dBm, the M-S chipless tag can provide up to 8 m sensing range with $P_t = 0$ dBm which is at least 2.5 times larger than what can be reached using the S-S chipless tag. This is a great improvement in vibration sensing performance provided by the extra vibration-induced modulation effect (near-field boundary modulation) included in the M-S chipless tag. Note that in terms of chipless tag detection range, the achieved result here is a 2.5 times range improvement over what was obtained based on Doppler modulation in [41] where the read range has been already increased by a factor of 10 compared to classical stationary chipless RFID. In addition, the PSD of the modulated backscattered signal from the vibrating M-S and S-S chipless tags $[S_r(f)]$ at their respective resonance frequencies are presented in Fig. 9 (c). Obviously, the large number of vibration harmonics (up to the 8th harmonic) can be easily detected with the M-S tag whereas the only first vibration harmonic is detectable with the S-S tag.

D. *Verification of the operational principle*

To clarify the exact physical phenomenon involved in the measurement process of the implemented vibrating M-S chipless tag, the modulated backscattered signal has been also experimentally studied in the time domain. The spectrum analyzer has been used in real-time mode with 1.28 kS/s sample rate to record the I/Q data associated with the backscattered signal for 0.4 sec which includes almost 23 vibration periods ($T_v = 1/58$ sec). Fig. 10 (a) presents the raw I/Q data captured by the spectrum analyzer for the M-S and S-S chipless tag at their respective resonance frequencies. Obviously, in Fig. 10 (a), the variation of the I/Q components associated with the M-S tag is certainly greater than those associated with the S-S tag. The statistical behavior of the modulated signal is studied using the histogram generated in the I-Q plane based on the 512 recorded samples of the signal as shown in Fig. 10 (b) and (c). In good agreement with the presented stochastic process model for the vibrating M-S chipless tag in Section II. D, as it is shown by the histogram in Fig. 10 (b), the signal samples are mostly concentrated around the two points in the I-Q plane which corresponds to the two main states of the vibrating M-S chipless tag. However, for the vibrating S-S chipless tag, the signal samples in the histogram shown in

Fig. 10 (c) are continuously varying in the I-Q plane along a much smaller path compared to that associated with M-S chipless tag shown in Fig. 10 (b). Finally, the I/Q diagram and magnitude/phase profile of the measured backscattered signal is respectively illustrated in Fig. 11 (a) and (b) during one vibration period [the 17th period in the Fig. 10 (a)] which are in accord with the theoretical results shown in Fig. 5. The modulated signal is mainly varying around the S1 and S2 points respectively shown in Fig. 11 (a) as $\gamma_1\, e^{j\psi_1}$ and $\gamma_2\, e^{j\psi_2}$, while the signal appears only four times around a third point which is considered as TS with $\gamma_3\, e^{j\psi_3}$ value. However, since the reflection from the environment is also included in the measurement results, the I/Q path of the backscattered signal from the vibrating tag can be arbitrarily transformed (translation and rotation transform) in the I-Q plane due to the contribution of the environment. Consequently, in contrast to the simulations, it is not possible to determine the dielectric layer (DL1 or DL2) with which the loop is in touch in each state (S1 and S2) based on the measurement results. In addition, note that since the measured I/Q data is just proportional to the scattering coefficients of the tag and not equal to that, the measured state values are presented with $\gamma_i\, e^{j\psi_i}$; $i = 1, 2, 3$ instead of $\rho_i\, e^{j\phi_i}$; $i = 1, 2, 3$. Based on the presented model and using a formulation similar to (5), the measured backscattered complex signal $s_r(t)$ can be written by considering the state values $\gamma_i\, e^{j\psi_i}$; $i = 1, 2, 3$ as

$$s_r(t) = \begin{cases} \gamma_1 e^{jk\psi_1} e^{j\beta \sin(\omega_v t)} & t \in q_1 \\ \gamma_2 e^{jk\psi_2} e^{j\beta \sin(\omega_v t)} & t \in q_2 \\ \gamma_3 e^{jk\psi_3} e^{j\beta \sin(\omega_v t)} & t \in q_3 \end{cases} \tag{14}$$

where $\omega_v = 2\pi \times 58$ rad/sec and β is calculated for the measurement with $D_v = 0.48$ mm and $f_0 = 4.74$ GHz. The results obtained based on (14) is compared with the measurement results in Fig. 11 (a) and (b) where both I/Q paths and the magnitude/phase profiles are in good agreement. The constant magnitude and partially sinusoidal phase variation of the measured backscattered signal from the vibrating M-S chipless tag during each state (S1 and S2) is verified experimentally based on results shown in Fig. 11 (b), which proves the presence of the near-field boundary modulation in the implemented vibrating M-S chipless tag.

E. Through-the-wall vibration sensing in a real environment

The improvement of the vibration sensing range and the sensing robustness which can be achieved using the presented M-S chipless tag is practically examined in a real environment with a through-the-wall measurement scenario. The same measurement bench as what has been introduced in Section III. B is used to organize the through-the-wall experimental setup shown in Fig. 12 where the loudspeaker with the attached chipless tags is located in one office room (office 1), and the RF signal generator, the spectrum analyzer and the RX/TX antennas (all with the same settings as what are mentioned in Section III. B i.e vertical polarization for antennas, $P_t = 0$ dBm, $f_0 = 4.5 : 0.01 : 5.3$ GHz, and $BW = 1$ kHz) are located in the other adjacent office room (office 2). The loudspeaker is fed by the LF signal generator

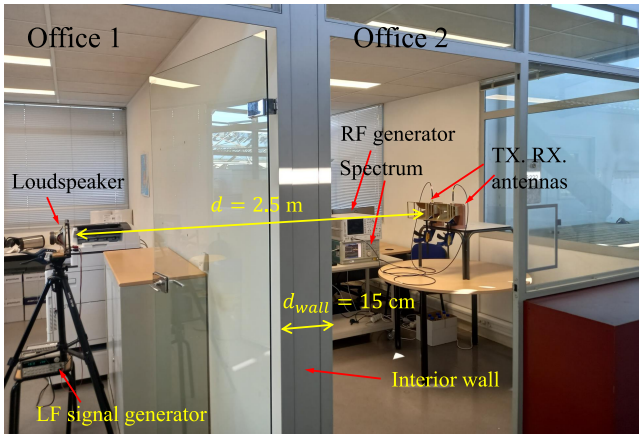

Fig. 12. Through-the-wall measurement scenario in a real indoor environment which consists of two office rooms.

(also located in office 1) with the same $f_v = 58$ Hz and $V_m = 2.5$ V which produce $D_v = 0.48$ mm vibration amplitude. The distance between the RX/TX antennas and the loudspeaker is set $d = 2.5$ m while a 15 cm thick wall ($d_{wall} = 15$ cm) exists at the middle of the backscattering path. The differential RCS of the vibrating loudspeaker is measured through the wall as a function of carrier frequency f_0 with the scenario already used in the anechoic chamber (Section III. C) and the results are presented in Fig. 13 (a). Comparing the results shown in Fig. 9 (a) and Fig. 13 (a), demonstrates that vibrating M-S chipless tag can be perfectly detected even through the wall and in the real environment, whereas the vibrating S-S chipless tag cannot be easily recognized. In fact, due to the multi-reflections caused by the wall and the multi-path effect in the real environment, some significant fluctuations appeared in the measured differential RCS profiles shown in Fig. 13 (a), which makes more difficult the detection of the vibrating tag. However, since the resonance peak level of the differential RCS for the vibrating M-S chipless tag at $f_0 = 4.74$ GHz is still almost 5 dB greater than the fluctuations peaks, the vibrating M-S chipless tag is well detected. In contrast, the resonance peak of the differential RCS for the vibrating S-S chipless tag at $f_0 = 5.01$ GHz is dominated with the fluctuation peaks level, and consequently, the detection of the S-S tag is impossible in this case. The measured PSD of the backscattered signal $S_r(f)$ at the corresponding resonance frequencies of the M-S and S-S chipless tags shown in Fig. 13 (b) clearly illustrate that the vibration harmonics (up to the 3rd harmonic) can be sensed through the wall and in a real environment from 2.5 m distance using the M-S chipless tag, while no harmonic is sensed with the S-S chipless tag. This result again highlights the fact that the Doppler modulation induced by the vibration with $D_v = 0.48$ mm at the low carrier frequency of $f_0 = 4.74$ GHz is such small that it cannot be detected in the real scenario at distances greater than 1 m, while of course, the presence of the wall barrier makes it absolutely impossible. However, the near-field modulation effect provided with the M-S chipless tag significantly increases the differential RCS so that the sub-millimeter vibration can be sensed even in the problematic

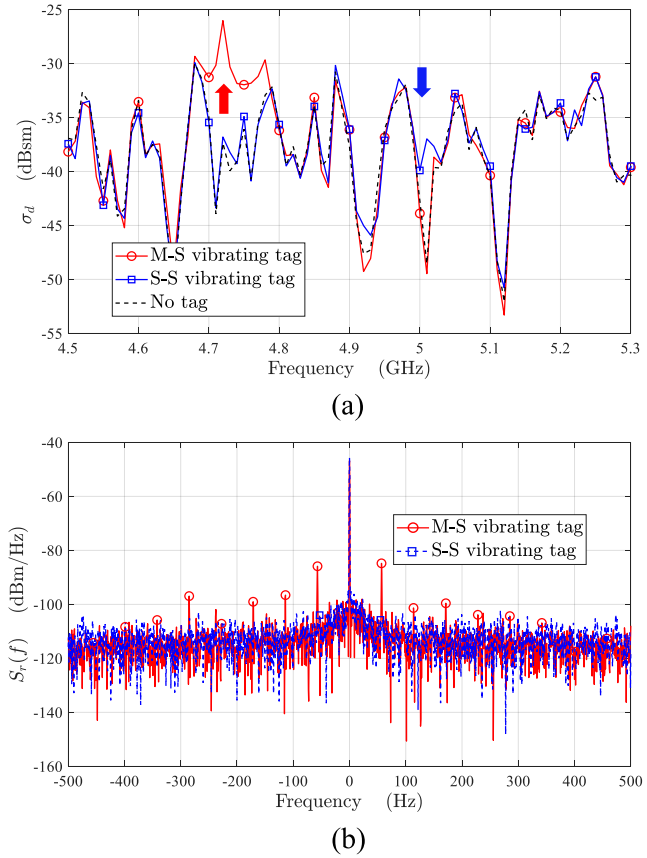

Fig. 13. (a) Through-the-wall measured differential RCS of the vibrating M-S and S-S chipless tags as a function of carrier frequency f_0. The case 'No tag' is for when the loop scatterer is not present on the loudspeaker. (b) Through-the-wall measured PSD of the modulated backscattered signal from the vibrating M-S and S-S chipless tag at their respective resonance frequencies.

practical situation at low microwave frequencies.

IV. Conclusion

The robust and relatively long-range vibration sensing method has been proposed based on the multi-state chipless RFID tags which are composed of resonant scatterers that are affected by the motion-induced near-field boundary modulation. The tag structure was designed and its behavior during vibration has been described with mechanical and electromagnetic models, which clearly demonstrates the involved physical concept. The presented multi-physics model has been verified using quasi-stationary full-wave simulations. The achieved enhancement in vibration sensing performance and potentially in identification capability has been explained based on the differential RCS which is analytically expressed for the vibrating multi-state chipless tag using a stochastic model. The prototype of the designed multi-state chipless tag has been implemented and all the proposed theoretical results have been proven in the measurements. The experimental results show an increase of a factor of 45 on the differential RCS which translates into an increase in read range of 2.5 compared to a classical chipless tag moving in the same way. Compared to a stationary chipless tag, the increase in the read range is a factor of 25. The sub-millimeter vibration has been perfectly detected at low microwave frequencies from large distances up to 2.5 m while the vibrating fully-passive multi-state chipless tag is located behind the wall in an indoor environment. In addition, the tag has been identified based on the observed resonance in the measured differential RCS profile. The presented concept can be effectively employed in human health and mechanical fault monitoring applications while the proposed low-cost multi-state chipless tags can be widely fabricated and used for these goals. This technique is also compatible for long-distance identification. In this case, as with stationary chipless tags, the amount of information is related to the number of resonators present in the tag and to the frequency band that can be dedicated to the application.

Acknowledgment

This work was supported by the European Research Council (ERC) through the European Union's Horizon 2020 Research and Innovation Program (ScattererID) under Grant N° 772539.

References

[1] F. C. Demarest, "High-resolution, high-speed, low data age uncertainty, heterodyne displacement measuring interferometer electronics," *Measurement Science and Technology*, vol. 9, no. 7, p. 1024, 1998.

[2] S. Donati, "Developing self-mixing interferometry for instrumentation and measurements," *Laser & Photonics Reviews*, vol. 6, no. 3, pp. 393–417, 2012.

[3] F. Michler, B. Scheiner, T. Reissland, R. Weigel, and A. Koelpin, "Micrometer sensing with microwaves: Precise radar systems for innovative measurement applications," *IEEE Journal of Microwaves*, vol. 1, no. 1, pp. 202–217, 2021.

[4] C. Gu, T. Inoue, and C. Li, "Analysis and experiment on the modulation sensitivity of Doppler radar vibration measurement," *IEEE microwave and wireless components letters*, vol. 23, no. 10, pp. 566–568, 2013.

[5] L. Piotrowsky and N. Pohl, "Spatially resolved fast-time vibrometry using ultrawideband FMCW radar systems," *IEEE Transactions on Microwave Theory and Techniques*, vol. 69, no. 1, pp. 1082–1095, 2020.

[6] Y. Yan, L. Cattafesta, C. Li, and J. Lin, "Analysis of detection methods of RF vibrometer for complex motion measurement," *IEEE transactions on microwave theory and techniques*, vol. 59, no. 12, pp. 3556–3566, 2011.

[7] C. Li and J. Lin, "Non-contact measurement of periodic movements by a 22-40GHz radar sensor using nonlinear phase modulation," in *2007 IEEE/MTT-S International Microwave Symposium*. IEEE, 2007, pp. 579–582.

[8] C. Li, V. M. Lubecke, O. Boric-Lubecke, and J. Lin, "A review on recent advances in Doppler radar sensors for noncontact healthcare monitoring," *IEEE Transactions on microwave theory and techniques*, vol. 61, no. 5, pp. 2046–2060, 2013.

[9] X. Ma, Y. Wang, L. Lu, X. Zhang, Q. Chen, X. You, J. Lin, and L. Li, "Design of a 100-GHz double-sideband low-IF CW Doppler radar transceiver for micrometer mechanical vibration and vital sign detection," *IEEE Transactions on Microwave Theory and Techniques*, vol. 68, no. 7, pp. 2876–2890, 2020.

[10] C. Li, X. Yu, D. Li, L. Ran, and J. Lin, "Software configurable 5.8 GHz radar sensor receiver chip in 0.13 μm cmos for non-contact vital sign detection," in *2009 IEEE Radio Frequency Integrated Circuits Symposium*. IEEE, 2009, pp. 97–100.

[11] G. Vinci, S. Lindner, F. Barbon, S. Mann, M. Hofmann, A. Duda, R. Weigel, and A. Koelpin, "Six-port radar sensor for remote respiration rate and heartbeat vital-sign monitoring," *IEEE Transactions on Microwave Theory and Techniques*, vol. 61, no. 5, pp. 2093–2100, 2013.

[12] C. Gu, Z. Peng, and C. Li, "High-precision motion detection using low-complexity Doppler radar with digital post-distortion technique," *IEEE Transactions on Microwave Theory and Techniques*, vol. 64, no. 3, pp. 961–971, 2016.

[13] A. D. Droitcour, O. Boric-Lubecke, V. M. Lubecke, J. Lin, and G. T. Kovacs, "Range correlation and I/Q performance benefits in single-chip silicon Doppler radars for noncontact cardiopulmonary monitoring," *IEEE Transactions on Microwave Theory and Techniques*, vol. 52, no. 3, pp. 838–848, 2004.

[14] C. Li and J. Lin, "Random body movement cancellation in Doppler radar vital sign detection," *IEEE Transactions on Microwave Theory and Techniques*, vol. 56, no. 12, pp. 3143–3152, 2008.
[15] C.-S. Lin, S.-F. Chang, C.-C. Chang, and C.-C. Lin, "Microwave human vocal vibration signal detection based on Doppler radar technology," *IEEE Transactions on Microwave Theory and Techniques*, vol. 58, no. 8, pp. 2299–2306, 2010.
[16] K. Han and S. Hong, "Vocal signal detection and speaking-human localization with MIMO FMCW radar," *IEEE Transactions on Microwave Theory and Techniques*, vol. 69, no. 11, pp. 4791–4802, 2021.
[17] X. Xiang, X. Zhang, and H. Chen, "Acquisition and enhancement of remote human vocal signals based on doppler radar," *IEEE Sensors Journal*, vol. 21, no. 18, pp. 20 348–20 361, 2021.
[18] M. Geiger, D. Schlotthauer, and C. Waldschmidt, "Improved throat vibration sensing with a flexible 160-GHz radar through harmonic generation," in *2018 IEEE/MTT-S International Microwave Symposium-IMS*. IEEE, 2018, pp. 123–126.
[19] Y. Zhang, S. Dong, C. Zhu, M. Balle, B. Zhang, and L. Ran, "Hand gesture recognition for smart devices by classifying deterministic Doppler signals," *IEEE Transactions on Microwave Theory and Techniques*, vol. 69, no. 1, pp. 365–377, 2020.
[20] D. Mascanzoni and H. Wallin, "The harmonic radar: a new method of tracing insects in the field," *Ecological entomology*, vol. 11, no. 4, pp. 387–390, 1986.
[21] K. Finkenzeller, *RFID handbook*. John wiley & sons, 2010.
[22] A. Singh and V. M. Lubecke, "Respiratory monitoring and clutter rejection using a CW Doppler radar with passive RF tags," *IEEE Sensors Journal*, vol. 12, no. 3, pp. 558–565, 2011.
[23] P. Li, Z. An, L. Yang, P. Yang, and Q. Lin, "RFID harmonic for vibration sensing," *IEEE Transactions on Mobile Computing*, vol. 20, no. 4, pp. 1614–1626, 2019.
[24] X. Hui and E. C. Kan, "Monitoring vital signs over multiplexed radio by near-field coherent sensing," *Nature Electronics*, vol. 1, no. 1, pp. 74–78, 2018.
[25] P. Sharma and E. C. Kan, "Sleep scoring with a UHF RFID tag by near field coherent sensing," in *2018 IEEE/MTT-S International Microwave Symposium-IMS*. IEEE, 2018, pp. 1419–1422.
[26] X. Hui, T. B. Conroy, and E. C. Kan, "Near-field coherent sensing of vibration with harmonic analysis and balance signal injection," *IEEE Transactions on Microwave Theory and Techniques*, vol. 69, no. 3, pp. 1906–1916, 2021.
[27] Y.-R. Ho and C.-L. Yang, "A wearable throat vibration microwave sensor based on split-ring resonator for harmonics detection," in *2020 IEEE/MTT-S International Microwave Symposium (IMS)*. IEEE, 2020, pp. 504–507.
[28] T.-C. Chang, P.-K. Chan, C.-H. Chen, K.-W. Chen, and C.-L. Yang, "Fingertip pulse signals enhanced by using intermodulation multiplication of active high-sensitivity split-ring resonator," in *2018 IEEE/MTT-S International Microwave Symposium-IMS*. IEEE, 2018, pp. 1416–1418.
[29] S. Tedjini, N. Karmakar, E. Perret, A. Vena, R. Koswatta, E. Rubayet *et al.*, "Hold the chips: Chipless technology, an alternative technique for RFID," *IEEE Microwave Magazine*, vol. 14, no. 5, pp. 56–65, 2013 .
[30] C. Herrojo, F. Paredes, J. Mata-Contreras, and F. Martín, "chipless RFID: A review and recent developments," *Sensors*, vol. 19, no. 15, p. 3385, 2019.
[31] L. Lasantha, N. C. Karmakar, and B. Ray, "Chipless RFID sensors for IoT sensing and potential applications in underground mining-A review," *IEEE Sensors Journal*, 2023 .
[32] N. Barbot, O. Rance, and E. Perret, "Classical RFID versus chipless RFID read range: Is linearity a friend or a foe?" *IEEE Trans. Microw. Theory Tech.*, vol. 69, no. 9, pp. 4199–4208, 2021 .
[33] E. Perret, "Displacement sensor based on radar cross-polarization measurements," *IEEE Transactions on Microwave Theory and Techniques*, vol. 65, no. 3, pp. 955–966, 2017.
[34] C. Herrojo, J. Mata-Contreras, F. Paredes, and F. Martín, "Microwave encoders for chipless RFID and angular velocity sensors based on S-shaped split ring resonators," *IEEE Sensors Journal*, vol. 17, no. 15, pp. 4805–4813, 2017.
[35] D. Girbau, Á. Ramos, A. Lazaro, S. Rima, and R. Villarino, "Passive wireless temperature sensor based on time-coded UWB chipless RFID tags," *IEEE Transactions on Microwave Theory and Techniques*, vol. 60, no. 11, pp. 3623–3632, 2012.
[36] F. Requena, M. Gilch, N. Barbot, D. Kaddour, R. Siragusa, F. Costa, S. Genovesi, and E. Perret, "Thermal modeling of resonant scatterers and reflectometry approach for remote temperature sensing," *IEEE Transactions on Microwave Theory and Techniques*, vol. 69, no. 11, pp. 4720–4734, 2021.
[37] A. Vena, E. Perret, D. Kaddour, and T. Baron, "Toward a reliable chipless RFID humidity sensor tag based on silicon nanowires," *IEEE Transactions on Microwave Theory and Techniques*, vol. 64, no. 9, pp. 2977–2985, 2016.
[38] F. Costa, A. Gentile, S. Genovesi, L. Buoncristiani, A. Lazaro, R. Villarino, and D. Girbau, "A depolarizing chipless RF label for dielectric permittivity sensing," *IEEE Microwave and Wireless Components Letters*, vol. 28, no. 5, pp. 371–373, 2018.
[39] A. Lazaro, R. Villarino, F. Costa, S. Genovesi, A. Gentile, L. Buoncristiani, and D. Girbau, "Chipless dielectric constant sensor for structural health testing," *IEEE Sensors Journal*, vol. 18, no. 13, pp. 5576–5585, 2018.
[40] A. Azarfar, N. Barbot, and E. Perret, "Motion-modulated chipless RFID," *IEEE Journal of Microwaves*, vol. 3, no. 1, pp. 256–267, 2022.
[41] ——, "Vibration sensing using Doppler-modulated chipless RFID tags," in *2022 IEEE MTT-S International Microwave Symposium (IMS)*, Denver, US, June 2022.
[42] ——, "Chipless RFID based on micro-Doppler effect," *IEEE Transactions on Microwave Theory and Techniques*, vol. 70, no. 1, pp. 766–778, 2021.
[43] J. Cooper and C. H. Wilcox, "Scattering by moving bodies: The quasi stationary approximation," *Math. Methods Appl. Sci.*, vol. 2, no. 2, pp. 131–148, 1980.
[44] P. Nikitin, K. Rao, and R. Martinez, "Differential RCS of RFID tag," *Electron. Lett.*, vol. 43, pp. 431 – 432, 02 2007.
[45] N. Barbot, O. Rance, and E. Perret, "Differential RCS of modulated tag," *IEEE Trans. Antennas Propag.*, vol. 2, no. 9, pp. 10–15, 2021.
[46] A. Voisin, A. Dumas, N. Barbot, and S. Tedjini, "Differential RCS of multi-state transponder," in *2022 Wireless Power Week (WPW)*. IEEE, 2022, pp. 195–198.

Ashkan Azarfar (Student Member, IEEE) received the B.Sc. from the Iran University of Science and Technology, Tehran, Iran in 2014, and the M.Sc. from the University of Tehran, Tehran, Iran in 2017, both in electrical engineering. He is currently pursuing the Ph.D. degree at the University of Grenoble Alpes, Grenoble INP, France.

His current research interests include motion-modulated chipless transponders, electromagnetic wave scattering, antenna design and wave propagation, and microwave circuits design.

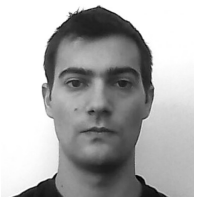

Nicolas Barbot (Member, IEEE) received the M.Sc. and Ph.D. degrees from the University de Limoges, France, in 2010 and 2013 respectively. His Ph.D. work in Xlim Laboratory, Limoges, France was focused on error-correcting codes for the optical wireless channel. He also realized a post-doctoral work in joint source-channel decoding at L2S Laboratory, in Gif-sur-Yvette, France. Since September 2014, he has been an Assistant Professor at the Université Grenoble Alpes - Grenoble Institute of Technology, in Valence, France. His scientific background at LCIS Laboratory, Valence, France covers wireless communications systems based on backscattering principle which include classical RFID and chipless RFID.

His research interests include transponders which can not be described by linear time-invariant systems. This gathers harmonic transponders which are based on the use of a non-linear component (Schottky diode) or linear time-variant transponders which are based on the modification of their response in the time domain. He also places special interests on antenna design and instrumentation based on these phenomenons.

Etienne Perret (Senior Member, IEEE) received the Eng. Dipl. degree in electrical engineering from the Ecole Nationale Supérieure d'Electronique, d'Electrotechnique, d'Informatique, d'Hydraulique, et des Télécommunications, Toulouse, France, 2002, and the M.Sc. and Ph.D. degrees in electrical engineering from the Toulouse Institute of Technology, Toulouse, in 2002 and 2005, respectively. From 2005 to 2006, he held a post-doctoral position with the Institute of Fundamental Electronics, Orsay, France. He was appointed Associate Professor in 2006 and Full Professor in 2022 of electrical engineering at Univ. Grenoble Alpes, Grenoble INP, France, where he heads the ORSYS Research Group (20 researchers) from 2015 to 2022. From 2014 to 2019, he has been a Junior Member with the Institut Universitaire de France, Paris, France, an institution that distinguishes professors for their research excellence, as evidenced by their international recognition. From 2015 to 2020, he has been an appointed Member of the French National Council of Universities. He has authored or co-authored more than 200 technical conferences, letters and journal papers, and books and book chapters. He holds several patents. His works have generated more than 4200 citations. His current research interests include wireless communication systems based on the principle of backscatter modulation or backscattering of EM waves especially in the field of RFID and chipless RFID for identification and sensors. His research interests also include electromagnetic modeling of passive devices for millimeter and submillimeter-wave applications, and advanced computer-aided design techniques based on the development of an automated codesign synthesis computational approach. Dr. Perret has been a Technical Program Committee member of the IEEE International Conference on RFID, the IEEE RFID TA; and currently he is a member of the IMS Technical Paper Review Committee. He was a recipient of several awards like the MIT Technology Review's French Innovator's under 35 in 2013, the French Innovative Techniques for the Environment Award in 2013, the SEE/IEEE Leon Brillouin Award for his outstanding achievement in the identification of an object in an unknown environment using a chipless label or tag in 2016, the IEEE MTT-S 2019 Outstanding Young Engineer Award, the Prix Espoir IMT – Académie des sciences in 2020 and the Grand Prix de l'Electronique Général Ferrié in 2021. He was a Keynote Speaker and the Chairperson of several international symposiums. Etienne Perret was awarded an ERC Consolidator Grant in 2017 for his project ScattererID.